CHEMISTRY OF MATERIALS

ARTICLE

pubs.acs.org/cm

Au−Cu_2O Core−Shell Nanoparticles: A Hybrid Metal-Semiconductor Heteronanostructure with Geometrically Tunable Optical Properties

Li Zhang,[§] Douglas A. Blom,[¶] and Hui Wang*[,§]

[§]Department of Chemistry and Biochemistry, [¶]Electron Microscopy Center and USC NanoCenter, University of South Carolina, Columbia, South Carolina 29208, United States

Supporting Information

ABSTRACT: Metal-semiconductor hybrid heteronanostructures may exhibit not only a combination of properties from the disparate components but also further enhanced property tunability and new synergistic properties that arise from the interactions between the metal and semiconductor components. Here we demonstrate that the Au−Cu_2O hybrid core−shell nanoparticles not only combine the optical signatures of Cu_2O nanoshells and the plasmonic properties of Au nanoparticles but exhibit further enhanced and expanded plasmonic tunability as well due to the dielectric properties of the Cu_2O shells surrounding the Au cores. We have developed a robust wet chemistry approach through which we can fine-control several important geometrical parameters of the Au−Cu_2O core−shell nanoparticles, such as Cu_2O shell thickness, size of the Au core, and the spacing between the core and shell, to systematically and selectively fine-tune the synergistic light absorption and scattering properties of the particles over a broad spectral range across the visible and near-infrared regions. We have further performed Mie scattering theory calculations to theoretically interpret the correlation between the geometrical parameters and optical characteristics of the Au−Cu_2O hybrid nanoparticles. Such optical tunability achieved through the fine-control over core and shell geometries is believed to be important to the optimization of the overall performance of hybrid heteronanostructure-based materials and/or devices for photonic, electronic, and optoelectronic applications.

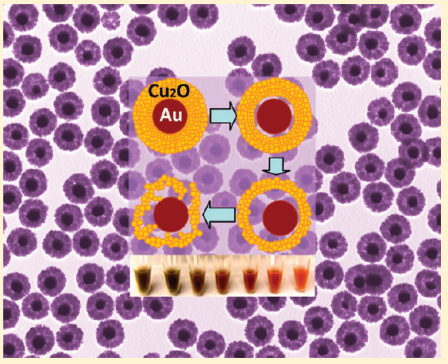

KEYWORDS: metal, semiconductor, hybrid nanoparticle, core−shell heteronanostructure, structure−property relationship, light absorption and scattering

INTRODUCTION

The past two decades have witnessed rapid advances in the colloidal synthesis of single-component metal and semiconductor nanoparticles,[1−4] which allow for the precise assembly of atoms into particles with well-controlled geometrical parameters. The capability to precisely maneuver both the particle dimensions and morphologies on the nanometer length-scale makes it possible to achieve a myriad of highly tunable physical and chemical properties by judiciously tailoring the nanoparticle geometry without changing the material composition. Such tunability may be further enhanced and/or expanded by expanding the materials systems from single-component nanoparticles to hybrid multicomponent heteronanostructures, which integrate discrete domains of different compositions within one hybrid nanostructured entity.[5−7] Metal-semiconductor hybrid nanoparticles represent an important class of multicomponent heterostructured nanosystems that may exhibit not only a combination of properties from the individual components but also, more interestingly, further enhanced property tunability and even new synergistic properties that arise essentially from the nanoscale interactions between the disparate metal and semiconductor components.[8]

Recent developments in colloidal nanoparticle synthesis allowed controllable preparation of a variety of hybrid metal-semiconductor nanostructures, such as metal-decorated anisotropic semiconductor nanoparticles,[9−15] nanoparticle heterodimers and dumbbell-like trimers,[16−19] and core−shell heterostructured nanoparticles,[20−29] with various compositional combinations and arrangements. A series of intriguing phenomena arising from the interactions between the nanoscale-spaced metal and semiconductor components have been observed in these hybrid heteronanostructures. It has been reported that the presence of metallic ingredients may significantly increase the photocatalytic and light-harvesting efficiencies by improving the charge separation at the semiductor-metal interfaces[12−14,19] and/or by enhancing the light absorption.[26] In addition, metallic components can alter the photoluminescence behaviors[9,21,23,27] and modify the nonlinear optical responses of the semiconductor components.[15,23,29] Furthermore, the presence of a semiconductor component in close proximity to a metallic nanostructure can also introduce interesting modifications to plasmonic features of the hybrid nanoparticle through plasmon-exciton coupling or alteration of the local dielectric environments.[21,23] Understanding how the

Received: July 20, 2011
Revised: September 3, 2011
Published: September 27, 2011

nanoscale metal-semiconductor interactions give rise to the tunable synergistic properties of hybrid heteronanostructures is directly related to our capabilities to selectively implement desired properties into hybrid nanomaterial systems for photonic, electronic, and optoelectronic applications.

Here we investigate, both experimentally and theoretically, the geometrically tunable optical properties of Au−Cu_2O hybrid core−shell nanoparticles. Au and Cu_2O represent an interesting combination of metal and semiconductor components for hybrid heteronanostructure construction. Au nanostructures possess geometry-dependent optical properties dominated by localized surface plasmon resonances, and such geometry-dependence of plasmon resonances has been demonstrated in a variety of nanoparticle geometries, such as nanorods,[30,31] nanoplates,[32] nanocages,[33] and nanoshells.[34,35] In addition to working directly with the nanoparticle geometries, the plasmonic features of a Au nanoparticle can also be systematically tuned through modification of the dielectric properties of its local environment.[36,37] Cu_2O, an important p-type semiconductor with interesting excitonic features,[38−44] possesses a set of unique optical and electronic properties appealing for photovoltaic[45−48] and photocatalytic applications.[49,50] Cu_2O nanostructures also exhibit geometrically tunable properties, which is one of the major reasons for the growing interest in a rapidly expanding array of Cu_2O nanoparticle geometries, such as nanospheres,[51−53] nanowires,[54] nanocubes,[55,56] nanopolyhedra,[57,58] and nanoshells.[59] In this paper, we demonstrate that the Au−Cu_2O hybrid core−shell nanoparticles combine the optical signatures of Cu_2O nanoshells in the visible and the tunable plasmon resonances of the Au nanoparticle cores in the near-infrared, both of which are sensitively dependent on the core and shell geometries. We have developed a robust wet chemistry approach, which involves the controllable growth of a polycrystalline Cu_2O nanoshell surrounding a Au nanoparticle core and the subsequent hollowing of the Cu_2O shell, to fine-control several important geometrical parameters of the Au−Cu_2O hybrid core−shell nanoparticles, such as Cu_2O shell thickness, size of the Au core, and the spacing between the core and shell. By adjusting these geometrical parameters, we can systematically fine-tune the synergistic optical properties of the Au−Cu_2O hybrid nanoparticles over a broad spectral range across the visible and near-infrared regions.

EXPERIMENTAL SECTION

All materials were used as received without further purification and ultrapure water (18.2 MΩ resistivity, Barnstead EasyPure II 7138) was used.

Synthesis of Au Nanoparticles. Au nanoparticles with two different sizes were synthesized and used as the core materials for Au−Cu_2O core−shell particle fabrication. Reducing chloroauric acid with formaldehyde at room temperature led to the formation of quasi-spherical Au nanoparticles with average radius of ∼63 nm. In a typical procedure, 50 mg of K_2CO_3 (J.T. Baker) was dissolved in 200 mL of water, followed by the addition of 3 mL of 25 mM $HAuCl_4$ (J.T. Baker). The mixture solution was aged in the dark for at least 12 h. Then 1.334 mL of formaldehyde solution (37 wt %, Sigma-Aldrich) was added into the mixture under vigorous magnetic stir (300 rpm). A brick-red colloidal suspension began to form after ∼15 min. The colloidal suspension was kept stirring for 30 min. Then Au nanoparticles were separated from the solution by centrifugation (2000 rcf), washed with polyvinylpyrrolidone (PVP, average M.W. 58000, Alfa Aesar) aqueous solution (20 g/L) and ethanol (Fisher Scientific) in sequence, and finally redispersed in 10 mL of water (final concentration of $\sim 6 \times 10^{10}$ particles/mL). Smaller Au nanoparticles with an average radius of ∼15 nm were synthesized following the previously reported citrate reduction protocol.[60] Briefly, 7.5 mL of 0.1 M sodium citrate (Fisher Scientific) solution was mixed with 150 mL of 0.25 mM $HAuCl_4$ in a 100 °C water bath under magnetic stir (300 rpm). The reaction mixture began to change color after ∼10 min and finally turned into a burgundy color after ∼15 min. The solution was kept stirring for 30 min, and then Au colloids were collected by centrifugation (8000 rcf), washed with water and ethanol, and finally redispersed in 7 mL of water (final concentration of $\sim 4 \times 10^{12}$ particles/mL).

Synthesis of Ag Nanoparticles. Silver colloid nanoparticles were synthesized by reducing the $[Ag(NH_3)_2]^+$ complex with glucose.[61] Briefly, 0.5 mL of 0.1 M $AgNO_3$ (Alfa Aesar) and 5 mL of 0.1 M ammonium solution (Fisher Scientific) were added into 43.5 mL of water under magnetic stir (300 rpm). 5.0 M NaOH (Fisher Scientific) solution was then added dropwise to adjust the pH to ∼13 followed by the introduction of 1 mL of 5 M glucose (Sigma-Aldrich) to initiate the formation of Ag nanoparticles, and the reaction mixture was kept stirring for 5 min. The Ag nanoparticles were centrifuged, washed with 20 g/L PVP solution and ethanol, and finally redispersed in 6 mL of water (final concentration of $\sim 7 \times 10^{11}$ particles/mL).

Synthesis of Au−Cu_2O Core−Shell Nanoparticles. 1.0 g of PVP was added to 50 mL of 0.01 M $Cu(NO_3)_2$ (Alfa Aesar) aqueous solution under constant magnetic stir (300 rpm). The solution was kept stirring for another 10 min to ensure that the PVP powders were completely dissolved. Then a certain amount of Au colloid solution was added, followed by immediate introduction of 17 μL of $N_2H_4 \cdot H_2O$ solution (35 wt %, Sigma-Aldrich) into the reaction mixture. The colloids changed colors from that of Au colloids into various characteristic colors of Au−Cu_2O core−shell nanoparticles typically within 10 s, and the final color of the colloids was found to be dependent on the volume of the Au colloid solution added. The reaction mixtures were stirred for 2 min, and then the Au−Cu_2O core−shell nanoparticles were washed with water and anhydrous ethanol and finally redispersed in ethanol and stored in refrigerator at 4 °C.

Synthesis of Rattle-like Au−Cu_2O Yolk-Shell Nanoparticles. The Cu_2O shells surrounding the Au cores were observed to undergo a symmetric hollowing process through which a cavity formed inside the Cu_2O shells, giving rise to the formation of rattle-like Au−Cu_2O yolk-shell nanoparticles. In a typical procedure, a colloidal solution of Au−Cu_2O core−shell nanoparticles was kept in the reaction mixture under magnetic stir at room temperature. The color of the colloid suspension was observed to change gradually over a time period of 1−2 h, indicating structural changes of the Au−Cu_2O hybrid nanoparticles. During the hollowing processes, we typically withdrew aliquots of colloidal solutions at certain reaction times from the reaction mixture, then immediately centrifuged the particles, washed them three times with water and ethanol, and finally redispersed them in ethanol. The samples were stored at 4 °C in refrigerator.

Synthesis of Ag−Cu_2O Hybrid Nanoparticles. The process of Ag−Cu_2O core−shell nanoparticle synthesis was similar to that of Au−Cu_2O core−shell nanoparticles. The fabrication procedures were basically the same, except that 2 mL of Ag colloid solution was added instead of the Au colloid solution. The hollowing of the Cu_2O shells surrounding the Ag core would also give rise to the formation of rattle-like Ag−Cu_2O yolk-shell nanostructures with controllable cavity sizes. The final products of Ag−Cu_2O core−shell nanoparticles and yolk-shell nanoparticles were also dispersed in ethanol and stored at 4 °C in refrigerator.

Characterizations. The crystalline structures of the nanoparticle samples were characterized by Powder X-ray Diffraction (PXRD) measurements which were performed at room temperature using a Rigaku D/Max 2100 Powder X-ray Diffractometer (Cu Kα1 radiation) with a

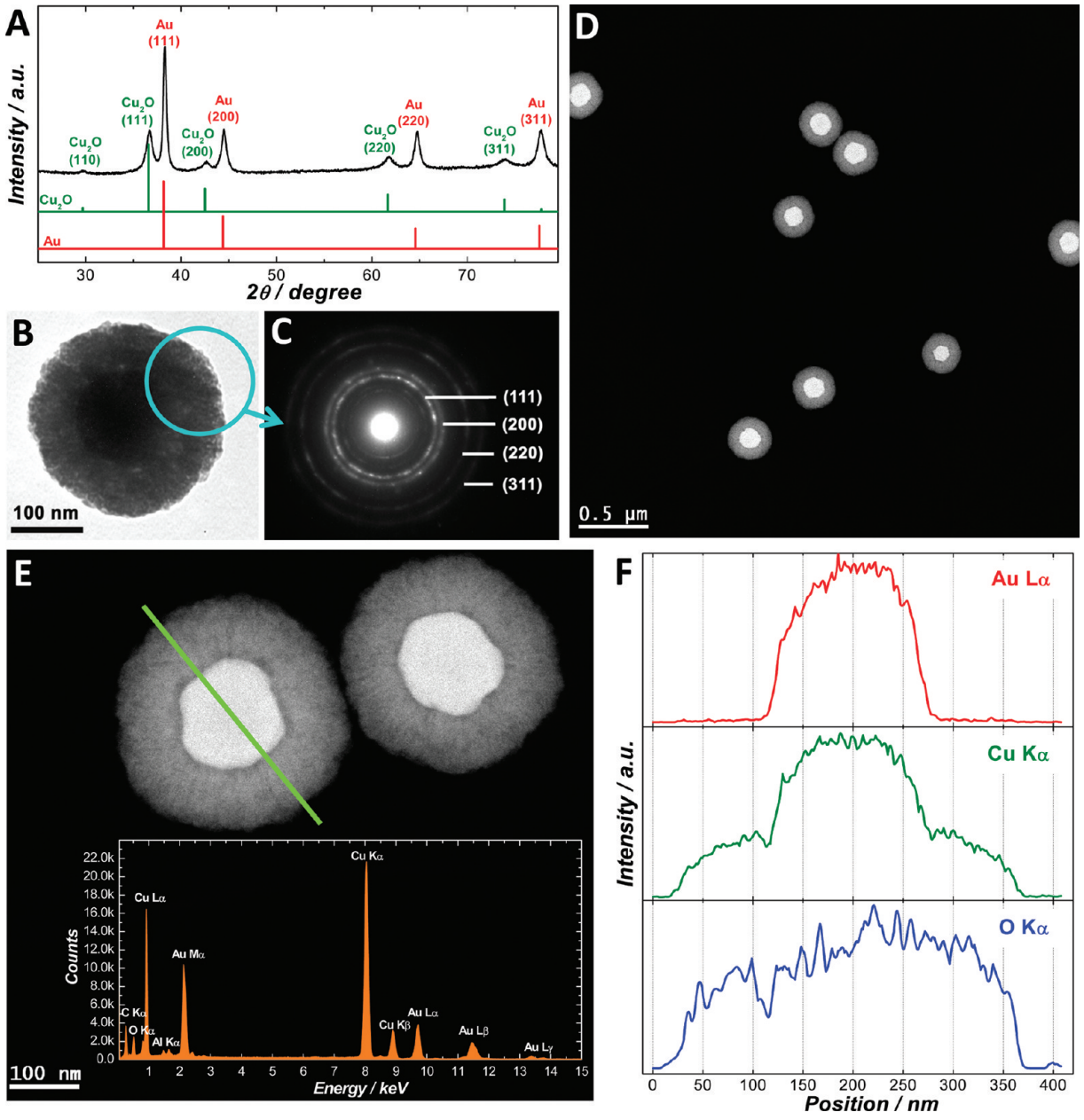

Figure 1. Structural characterizations of Au−Cu_2O core−shell nanoparticles. (A) PXRD patterns of Au−Cu_2O core−shell nanoparticles together with the standard diffraction patterns for cubic-phase Au and Cu_2O. (B) Bright-field TEM image of an individual Au−Cu_2O nanoparticle. (C) SAED pattern obtained from the Cu_2O shell region indicated as a circle in panel B. (D) HAADF-STEM image of Au−Cu_2O nanoparticles. (E) High-magnification HAADF-STEM image of two Au−Cu_2O nanoparticles and (*inset*) an integrated EDX spectrum obtained through line-scan along the green-line as indicated. (F) Spatial elemental distribution obtained from the EDX line-scan measurements based on Au Lα, Cu Kα, and O Kα lines.

diffracted beam graphite monochromator. The morphologies and structures of the nanoparticles were characterized by bright-field Transmission Electron Microscopy (TEM) and Selected Area Electron Diffraction (SAED) measurements using a Hitachi H-8000 transmission electron microscope operated at an accelerating voltage of 200 kV. For TEM and SAED measurements, all samples were dispersed in ethanol and drop-dried on 200 mesh Formvar/carbon coated Cu grids.

More detailed structural information was obtained by performing Scanning Transmission Electron Microscopy (STEM) and Energy Dispersed X-ray Spectroscopy (EDX) measurements using a JEOL 2100F 200 kV FEG-STEM/TEM equipped with a CEOS C_s corrector on the illumination system. The nanoparticles suspended in ethanol were placed dropwise and dried on a 200 mesh Cu TEM grid with a thin amorphous holey carbon support film. In STEM measurements, the geometrical aberrations were measured and controlled to provide less than a $\pi/4$ phase shift of the incoming electron wave over the probe-defining aperture of 15.5 mrad which at 200 kV provides a nominal probe size of 0.1 nm. High-Angle Annular Dark-Field Scanning Transmission Electron Microscopy (HAADF-STEM) images were acquired on a Fischione Model 3000 HAADF detector with a camera length such that the detector spanned 50−284 mrad. The scanning acquisition was synchronized to the 60 Hz AC electrical power to minimize 60 Hz noise in the images, and a pixel dwell time of 16 μs was chosen. Spatially resolved line-scans across the nanoparticles were acquired with a high current probe of 500 pA and nominal probe size of 0.5 nm with a probe angle of 25 mrad. A solid-state Si(Li) X-ray detector from Oxford

dx.doi.org/10.1021/cm202078t |*Chem. Mater.* 2011, 23, 4587–4598

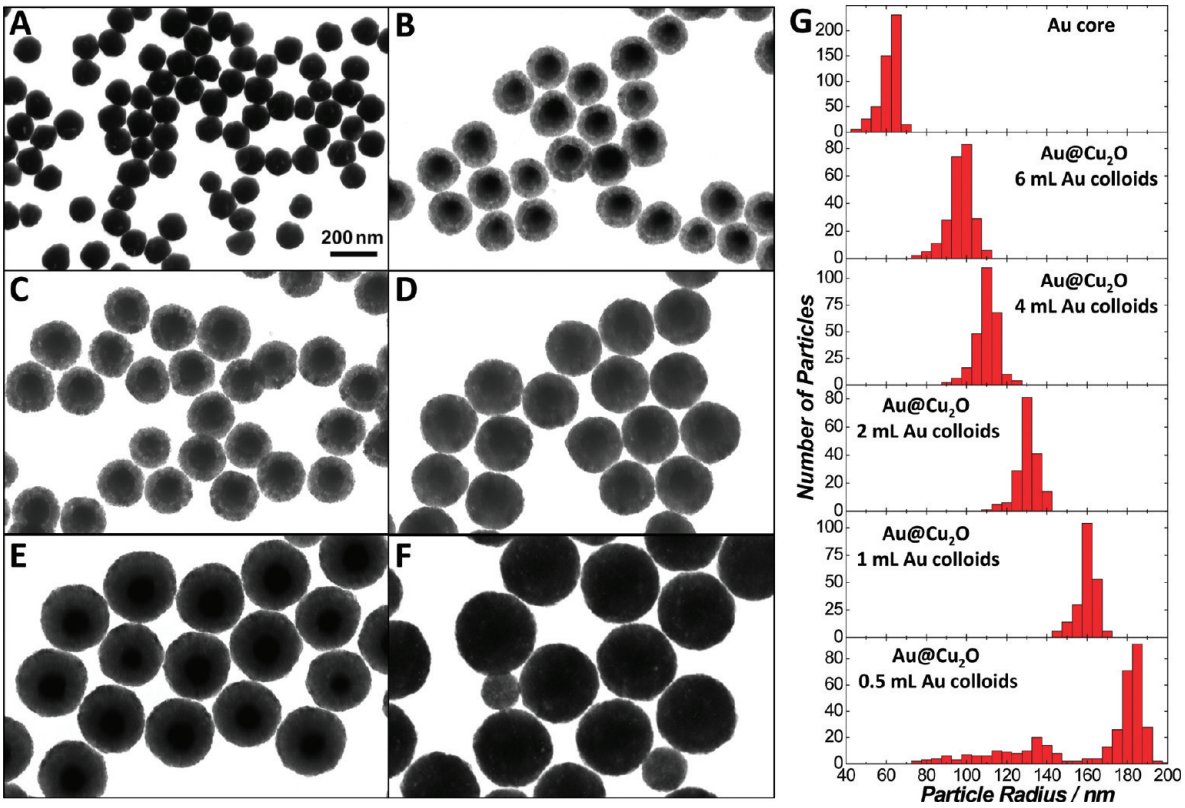

Figure 2. Au−Cu_2O core−shell nanoparticles with tunable Cu_2O shell thicknesses. Bright-field TEM images of (A) Au nanoparticles and Au−Cu_2O core−shell nanoparticles with various shell thicknesses obtained by adding different volumes of Au colloids: (B) 6 mL; (C) 4 mL; (D) 2 mL; (E) 1 mL; and (F) 0.5 mL. (G) Size distribution histograms of Au nanoparticles and Au−Cu_2O core−shell nanoparticles with various shell thicknesses. All TEM images share the same scale-bar in panel A.

Instruments was used to collect the EDX data. The probe was stepped across the sample with a spacing of 2 nm and a dwell time at each pixel of 0.5 s. A full EDX spectrum was acquired at each probe position. An energy window appropriate for the element of interest was defined, and line-scans were extracted from the EDX data.

The optical properties of the nanoparticles were studied by performing UV−visible-near-infrared extinction spectroscopy measurements on aqueous colloidal suspensions in a 1 cm-path length quartz cuvette using a Beckman coulter Du 640 spectrophotometer at room temperature.

RESULTS AND DISCUSSION

We recently reported that Cu_2O nanocrystallites would self-assemble into a mesoscopic spherical particle in the presence of polyvinylpyrrolidone (PVP) as a structural directing agent.[59] Here we found that Au nanoparticles could serve as the seeds to mediate the hierarchical assembly of Cu_2O nanocrystallites, which gave rise to the formation of a polycrystalline Cu_2O nanoshell wrapping around the Au core. Our approach is drastically different from the epitaxial growth approach which is currently the most extensively used method for the fabrication of multicomponent heteronanostructures. For metal and semiconductor pairs with large lattice mismatches, the direct epitaxial overgrowth of monocrystalline semiconductor nanoshells surrounding metallic nanoparticle cores remains challenging, and alternative novel nonepitaxial approaches need to be developed to overcome the obstacle of lattice-matching constraint.[25] Nevertheless, there are recent, successful attempts to epitaxially grow compact, single-crystalline Cu_2O shells on the surface of highly faceted or quasi-spherical Au nanoparticles due to the relatively small lattice mismatch between Au and Cu_2O (4.5%), and the shape and crystalline facets of the Au core were found to be well preserved in the resulting Cu_2O shells with faceted outer surfaces.[62−65] In contrast to those single-crystalline Cu_2O shells, the Cu_2O shells surrounding the Au cores obtained using our method were apparently polycrystalline in nature, composed of a large number of randomly orientated, small Cu_2O nanocrystallites.

Structural Characterizations of Au−Cu_2O Core−Shell Nanoparticles. Figure 1A shows the PXRD pattern of a Au−Cu_2O core−shell nanoparticle sample obtained by introducing 2 mL of 63 nm-radius Au colloids as the seeds for the growth of Cu_2O shells. The PXRD pattern of this sample clearly indicates that the as-fabricated core−shell nanoparticles were composed of pure cubic-phase Au (PDF # 98−000−0230) and Cu_2O (PDF # 03−065−3288) with lattice constants of 4.08 and 4.25 Å, respectively. The PXRD peaks from Cu_2O were significantly broadened largely due to the small size of the primary Cu_2O nanocrystallites in the shells. Figure 1B shows a bright-field TEM image of an individual nanoparticle with different contrast between the core and shell based on which its core radius and shell thickness were determined to be ~63 nm in ~67 nm, respectively. The SAED pattern (Figure 1C) recorded on the Cu_2O shell region as indicated by the blue circle in Figure 1B further verified that the Cu_2O nanoshell was polycrystalline in nature and consisted of cubic-phase Cu_2O nanocrystallites randomly oriented in the shell. The concentric diffraction rings from inside to outside in Figure 1C were indexed to be corresponding to the (111), (200), (220), and (311) planes of

dx.doi.org/10.1021/cm202078t |*Chem. Mater.* 2011, 23, 4587–4598

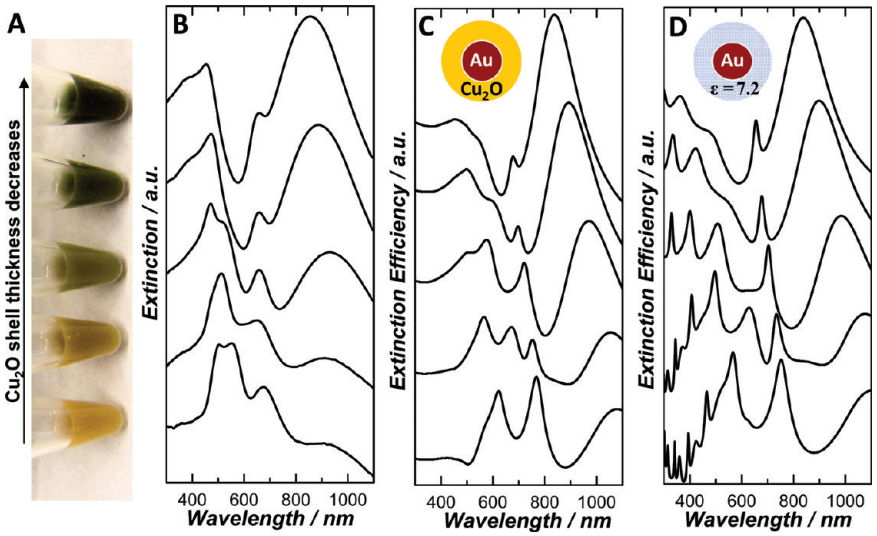

Figure 3. Optical properties of Au−Cu_2O core−shell nanoparticles. (A) Photograph of colloidal suspensions of Au−Cu_2O core−shell nanoparticles with varying average Cu_2O shell thicknesses of 35 nm, 47 nm, 67 nm, 97 nm, and 120 nm (*from top to bottom*). (B) Experimentally measured extinction spectra of the five colloidal samples shown in panel A. (C) Calculated extinction spectra of a Au−Cu_2O core−shell nanoparticle with varying Cu_2O shell thickness. The radius of Au core is fixed at 63 nm, and the outer radius of Au−Cu_2O core−shell particle is 98 nm, 110 nm, 130 nm, 160 nm, and 183 nm (*from top to bottom*). A 1 nm-gap between the Au core and Cu_2O shell is included and is filled with H_2O to better mimic the real geometry of the experimentally fabricated particles. The surrounding medium outside the Au−Cu_2O core−shell nanoparticles is H_2O. (D) Calculated extinction spectra of a Au nanoparticle encapsulated by a dielectric shell ($\varepsilon = 7.2$) with the same geometrical parameters as the Au−Cu_2O particle shown in panel C except that the Cu_2O shell is replaced by a dielectric shell.

pure cubic phase of Cu_2O respectively, which was in agreement with the PXRD results. No SAED feature corresponding to metallic Cu or cupric oxide (CuO) was observed.

The core−shell dimensions and interfacial structures can be resolved in greater detail by HAADF-STEM imaging (Figure 1D), which provided clearer contrast between the core and shell than bright-field TEM. It was apparent that each core−shell nanoparticle only contained one individual Au nanoparticle core, and almost no particles with multiple Au cores or without a Au core were found in this sample. The as-obtained core−shell nanoparticles exhibited uniform spherical overall morphology, well-preserving the quasi-spherical shape of the Au cores. In the high-magnification HAADF-STEM image shown in Figure 1E, a roughly 1 nm-gap between the Au core and Cu_2O shell could be clearly seen, possibly due to the presence of a thin layer of PVP adsorbed on the outer surface of the Au core nanoparticles. We have further performed line-scanned element analysis on individual core−shell nanoparticles using EDX spectroscopy. The inset of Figure 1E shows an integrated EDX spectrum along the green-line across an individual core−shell particle, which clearly shows the presence of Au, Cu, and O. The EDX line-scanning results (Figure 1F) revealed that Au was strictly confined in the central core area, while Cu and O, on the contrary, were distributed over the whole cross-section of core−shell particle. It is noteworthy that the Cu line-scans were a combination of the directly excited Cu X-rays from the sample and indirectly excited X-rays from the Cu grid bars (25 μm thick), and the proportion of Cu X-rays from the sample and the grid was variable across the line-scans and could not be separated. The significant increase in the amount of Cu in the Au core region was largely due to the contribution from the signals of the Cu grid underneath the particle, which was significantly enhanced when strong electron scattering from the Au core occurred during the line-scan process.

Tuning Optical Properties by Adjusting Cu_2O Shell Thickness. Our approach provides a unique way to fine-control the thickness of Cu_2O shells over a broad size range while well-maintaining the symmetry and spherical overall morphology of the particles even in the thick Cu_2O shell regime. In a typical procedure, varying volumes of Au colloidal solution were introduced into the reaction mixtures containing fixed initial concentrations of Cu^{2+} and PVP such that Au−Cu_2O core−shell nanoparticles with fixed core size but varying outer shell dimensions could be obtained. Figure 2A-F shows the bright-field TEM images of the quasi-spherical Au core nanoparticles (average radius of 63 nm) and Au−Cu_2O core−shell nanoparticle samples with five different average shell thicknesses obtained by introducing 6, 4, 2, 1, and 0.5 mL of Au seed solution, respectively. Relatively narrow single Gaussian peaks were displayed in the particle size distribution histograms shown in Figure 2G. The average particle radii were determined from the mean value of Gaussian distributions to be 98 nm, 110 nm, 130 nm, 160 nm, and 183 nm, which corresponded to average Cu_2O shell thickness of 35 nm, 47 nm, 67 nm, 97 nm, and 120 nm, respectively.

The outer radii of the core−shell particles were observed to progressively increase as the volume of colloidal Au seeds decreased. In principle, one should be able to approach the extreme thick shell regime by further decreasing the volume of Au seed solution. However, the coexistence of single-component Cu_2O particles at low Au to Cu_2O ratios set the limit of the shell thickness tuning range to be within roughly 120 nm using the present approach. It was observed that when the volume of Au colloids decreased to 0.5 mL, in addition to Au−Cu_2O core−shell nanoparticles (accounts for ~85%), a new subpopulation (accounts for ~15%) corresponding to smaller Cu_2O particles without any Au cores also began to develop, as shown in Figure 2F and the bottom panel in Figure 2G. Further decrease in the volume of Au seed particles would give rise to further

dx.doi.org/10.1021/cm202078t |*Chem. Mater.* 2011, 23, 4587–4598

increased fraction of single-component Cu_2O particles without Au cores primarily due to the fact that there were not enough Au seed particles to mediate the formation of Cu_2O shells, thereby leading to the self-aggregation of Cu_2O nanocrystallites without encapsulating the Au cores.

The as-fabricated Au−Cu_2O core−shell nanoparticles exhibited highly tunable optical properties in the visible and near-infrared regions, which were sensitively dependent on the Cu_2O shell thickness. Figure 3A shows a photograph of colloidal solutions of core−shell nanoparticles (see TEM images of these samples in Figure 2B−F). The color of colloidal solutions varied from yellow all the way to dark green as the thickness of Cu_2O shells decreased. The corresponding experimental extinction (absorption + scattering) spectra shown in Figure 3B exhibited much more complicated optical features in comparison to either Cu_2O nanoshells or Au nanoparticles. The spectral features on the blue side of 600 nm shared similarities with the optical characteristics of Cu_2O nanoshells in terms of the multipeaked extinction line-shapes and red-shift of peaks when the shell thickness increased. These features were primarily arising from geometry-dependent light absorption and scattering from the mesoscopic Cu_2O nanoshells.[59] The spectral features on the red side of 600 nm could be most reasonably assigned to the plasmon resonances of Au cores whose frequencies red-shifted from ~600 nm for the bare Au nanoparticles (see Figure S1 in the Supporting Information) all the way into near-infrared at wavelengths beyond ~1000 nm when the Au cores were wrapped inside the Cu_2O shells. The plasmon resonance frequencies were observed to be sensitively dependent on the thickness of Cu_2O shells, progressively shifting to longer wavelengths as the Cu_2O shells became thicker.

The nanoparticle plasmon resonances progressively red-shift as the refractive index of the surrounding medium increases.[37] It has been previously reported that coating the Au or Ag nanoparticle surfaces with a SiO_2 dielectric nanoshell led to the red-shift of the nanoparticle plasmon resonances over several tens of nanometers in wavelength simply due to the increased refractive index of SiO_2 (1.43) in comparison to that of H_2O (1.33).[66−69] Here the surprisingly large red-shift of plasmon resonances of Au over several hundred nanometers in wavelength was primarily due to the high refractive index of Cu_2O (~2.7 at wavelengths above 600 nm).[70] As shown in Figure S2 in the Supporting Information, bulk Cu_2O is a semiconducting material with interesting dielectric functions that are dramatically different from those of metals, such as Au and Ag.[71] At wavelength range below ~700 nm, both the real part and imaginary part of Cu_2O's dielectric functions change dramatically as wavelength varies largely due to the excitonic interband transitions of Cu_2O. As previously demonstrated in great detail, the unique dielectric functions of Cu_2O in this spectral range, together with the nanoshell geometry, determine the geometry-dependent light absorption and scattering signatures of Cu_2O nanoshells in the visible region.[59] At wavelengths longer than ~700 nm, the real part of dielectric function reaches a plateau around a positive constant of ~7, while the imaginary part of dielectric function becomes very close to 0. Therefore, Cu_2O is optically more like a dielectric material in the near-infrared with high refractive index, which is responsible for the large red-shift of Au plasmon resonances observed in these Au−Cu_2O hybrid core−shell nanoparticles. Although the core and shell may not be in direct contact, the ~1 nm-gap between the core and shell is very small in comparison to the decay length of the local field enhancements

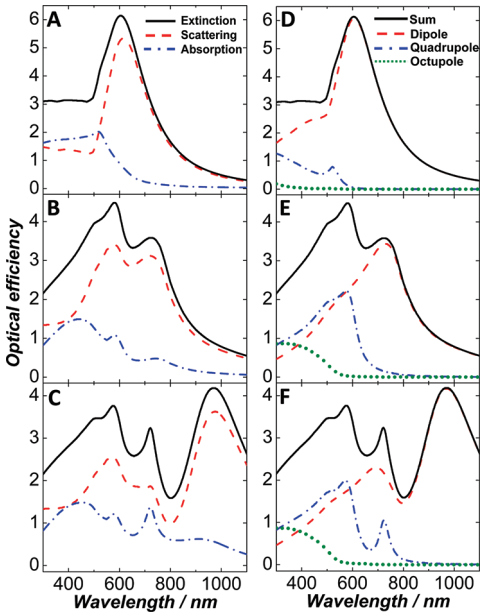

Figure 4. Calculated absorption, scattering, and extinction spectra of (A) a spherical Au nanoparticle (63 nm in radius), (B) a Cu_2O nanoshell with inner and outer radii of 64 and 130 nm respectively, and (C) a Au−Cu_2O core−shell particle with a core radius of 63 nm and an outer radius of 130 nm. A 1 nm-gap between the Au core and Cu_2O shell is included. The dielectric medium in interior cavities and surrounding the outer surface of the particles is assumed to be H_2O. The calculated absorption, scattering, and extinction include dipole, quadrupole, and octupole resonances. Calculated dipolar, qudrupolar, octupolar, and sum extinction spectra of (D) a spherical Au nanoparticle (63 nm in radius), (E) a Cu_2O nanoshell with inner and outer radii of 64 and 130 nm respectively, and (F) a Au−Cu_2O core−shell particle with a core radius of 63 nm and an outer radius of 130 nm.

associated with the plasmonic excitation of the Au core. Therefore, the plasmon resonances of the Au cores are still significantly red-shifted due to the high refractive index of the Cu_2O shells in spite of the presence of the gap.

Mie Scattering Theory Calculations. To gain further insights into the spectral complexity and optical tunability of the Au−Cu_2O hybrid core−shell nanoparticles, we theoretically calculated scattering, absorption, and extinction spectra of the nanoparticles using Mie scattering theory.[72] In these calculations, we assumed spherically symmetric core−shell geometry with geometrical parameters and compositions matching the experimentally fabricated nanoparticles. The wavelength-dependent empirical dielectric functions of bulk Cu_2O,[70] Au,[71] and Ag[71] shown in Figure S2 in the Supporting Information were used, and the dielectric medium surrounding the outer surface of the particles was water (refractive index of 1.33). In order to better mimic the exact geometry of the experimentally fabricated particles, a 1 nm-gap was added between the Au core and Cu_2O shell, which was also filled with water. The calculated absorption, scattering, and extinction were expressed as optical efficiencies, which were the ratio of the energy scattered or absorbed by the particle to the energy incident on its physical cross section.

Figure 3C shows the calculated extinction spectra of Au−Cu_2O core−shell nanoparticles with a fixed core radius of 63 nm and a varying outer radius of 98 nm, 110 nm, 130 nm, 160 nm, and 183 nm. The calculated extinction spectra exhibit multipeaked spectral features in the visible and near-infrared which all

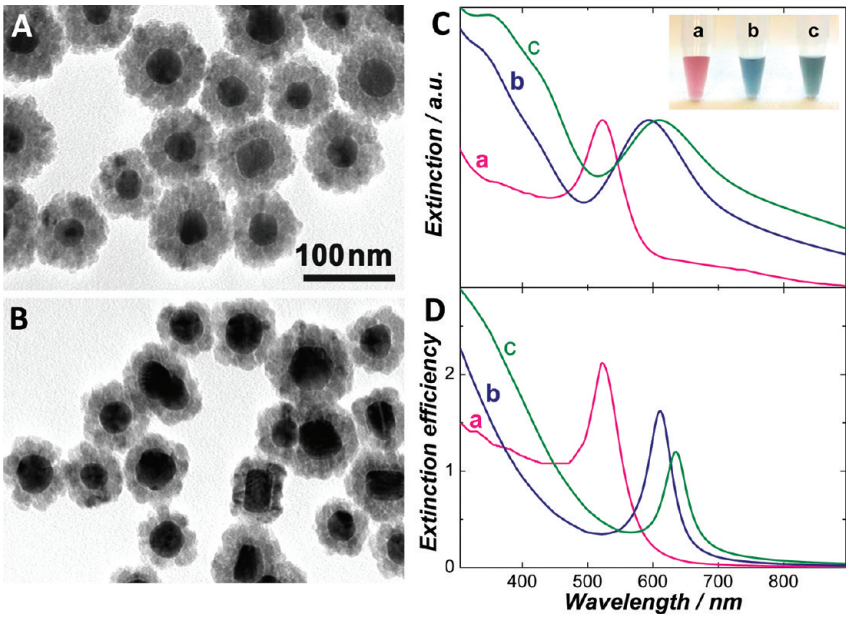

Figure 5. Optical properties of Au−Cu_2O core−shell nanoparticles within quasi-static limit. Bright-field TEM images of Au−Cu_2O core−shell nanoparticles obtained by adding (A) 2 mL and (B) 4 mL of citrate Au colloids (average diameter of 30 nm). (C) Experimental extinction spectra of (a) citrate-Au colloids, (b) Au−Cu_2O core−shell nanoparticles shown in panel B, and (c) Au−Cu_2O core−shell nanoparticles shown in panel A. The inset is a photograph of the colloidal samples. (D) Calculated extinction spectra of (a) a Au sphere, 15 nm in radius, (b) a Au−Cu_2O core−shell nanoparticle with 15 nm core radius and 27 nm outer radius, and (c) a Au−Cu_2O core−shell nanoparticle with 15 nm core radius and 40 nm outer radius. A 1 nm-gap between the Au core and Cu_2O shell is included.

progressively red-shift as the thickness of the Cu_2O shell increases. The overall line-shape and peak positions in the calculated extinction spectra match the experimental spectra reasonably well. The red-shift of Au plasmon resonances is primarily due to Cu_2O's high refractive index in the near-infrared. To further verify this, we have calculated extinction spectra of a Au nanoparticle surrounded by a dielectric shell (ε = 7.2) with exactly the same set of geometrical parameters as the Au−Cu_2O core−shell particles shown in Figure 3C. As shown in Figure 3D, the extinction features of the Au-dielectric core−shell nanoparticles exhibit very similar characteristics as Au−Cu_2O core−shell nanoparticles at wavelengths longer than 700 nm, strongly indicating that the near-infrared extinction features are arising from the plasmon resonances of the Au core and the large red-shift of Au plasmons observed in the hybrid core−shell nanoparticles is indeed due to the high refractive index of the Cu_2O shell. In the visible region, however, the extinction line-shapes of this Au-dielectric core−shell particle are dramatically different from those of the Au−Cu_2O core−shell nanoparticle due to the difference in dielectric functions of the shell materials. The multiple sharp peaks in the wavelength range from 300 to 600 nm are characteristics of light scattering at Mie resonance frequencies from the mesoscopic metal-dielectric core−shell particles.[73]

The multipeaked extinction line-shape and spectral tunability of the Au−Cu_2O core−shell nanoparticles observed in the present study are essentially arising from combined contributions from the geometry-dependent light absorption and scattering from the particles. As shown in Figure 4A and B, the extinction features of both a Au nanosphere (63 nm in radius) and a Cu_2O nanoshell (inner radius of 64 nm and outer radius of 130 nm) are dominated by scattering rather than absorption in the visible spectral region due to their relatively large sizes. Only within the spectral regions where interband transitions of Au and Cu_2O occur can a significant increase in the absorption efficiency be observed. Figure 4C shows the calculated absorption and scattering spectra of a Au−Cu_2O core−shell particle with core radius of 63 nm and outer radius of 130 nm. It is apparent that the extinction spectrum of this core−shell nanoparticle is not a simple linear combination of the optical features of its Au and Cu_2O components but indeed exhibits new synergistic optical characteristics with absorption and scattering features further expanded and red-shifted from visible into near-infrared. Since these particles are no longer in the small size regime within the quasi-static limit, phase-retardation effects become significant.[74,75] Therefore in addition to dipolar resonances, higher order mulitpolar resonances, such as quadrupole and octupole, also show significant contributions to the overall extinction of the particles. In Figure 4D-F, we further decomposed the extinction of the nanoparticles into dipolar, quadrupolar, octupolar components, each of which has its own characteristic resonance frequencies and line-shapes and, accordingly, contributes to the complexity of the overall extinction line-shape. These results further verify that near-infrared peaks observed in the extinction spectra of Au−Cu_2O core−shell nanoparticles correspond to the plasmon resonances from the Au nanoparticle cores, while the multipeaked features in the visible are from the Cu_2O nanoshells. The two extinction peaks in the near-infrared apparently correspond to the dipolar and quadrupolar plasmon resonances, respectively. In principle, the excitons in the Cu_2O shell might also be expected to couple with the plasmon resonances of the core, giving rise to double-peaked plasmonic features in extinction spectra. However, the double peaks in the near-infrared observed here are much less likely to be a feature of plasmon split due to plasmon-exciton coupling in these core−shell hybrid nanoparticles because of two major reasons. First, the plasmon resonances of Au core are shifted into near-infrared,

dx.doi.org/10.1021/cm202078t |*Chem. Mater.* 2011, 23, 4587–4598

far away from the visible region (above 2.2 eV) where interband transitions of Cu_2O occur. Second, the excitons of Cu_2O are so significantly broadened at room temperature that no obvious coupling between the discrete excitons and the plasmons is expected to be observable under the current experimental conditions.[76]

Small Au−Cu_2O Core−Shell Nanoparticles within Quasi-Static Limit: Effects of Particle Size. Using the current approach, we could also grow polycrystalline Cu_2O nanoshells using citrate-Au colloids (average diameter of 30 nm) as the core material to fabricate smaller Au−Cu_2O core−shell nanoparticles within the quasi-static limit. As shown in Figure 5, by varying the relative ratio between Cu_2O precursors and Au colloids, we could control the Cu_2O shell thickness to achieve tunable optical properties in the visible spectral region. The citrate-Au colloids showed a well-defined dipolar plasmon resonance at ~520 nm, which shifted to longer wavelengths upon the formation of Cu_2O nanoshells surrounding the Au cores, giving rise to dramatic changes in the color of colloidal solutions as seen in the inset of Figure 5C. The calculated extinction spectra of these nanoparticles (Figure 5D) were in good agreement with the experimental spectra. In analogy to the larger particles beyond the quasi-static limit, the plasmon resonance frequencies of these small nanoparticles were also sensitively dependent on the Cu_2O shell thickness. However, the plasmon tuning range of these small particles turned out to be much narrower than the bigger particles largely due to the fact that the local electromagnetic field enhancements associated with plasmon excitations decay over a much shorter length-scale for the smaller particles in comparison to the bigger particles.[67] The current approach also set a limit for the shell thickness tuning range for these small nanoparticles, typically in the range from ~10 nm to ~50 nm. Growing thin Cu_2O nanoshells within the sub-10 nm thickness regime surrounding the citrate-Au colloids turned out to be challenging simply because of the finite size limit of individual Cu_2O nanocrystallites in the shells.

Figure 6A-C shows the calculated absorption and scattering spectra of an individual Au nanoparticle (15 nm radius) and Au−Cu_2O core−shell nanoparticle with varying shell thicknesses. In striking contrast to the bigger particles beyond the quasi-static limit, the extinction spectra of these small nanoparticles are dominated by absorption with very small contributions from scattering. In addition, as shown in Figure 6D-F, the plasmon resonances in the visible spectral region are almost purely dipolar in nature with negligible contribution from high-order multipolar resonances. As a consequence, these small nanoparticles exhibit much simpler extinction line-shapes in comparison to the bigger particles. Furthermore, the geometrically tunable light scattering features from mesoscopic Cu_2O nanoshells were no longer observed in the visible region, and only an absorption edge below ~400 nm, which was the optical characteristics of small Cu_2O nanoparticles or nanoshells within the quasi-static limit,[59,76] was displayed in the extinction spectra.

Taken together, our approach for the controllable fabrication of Au−Cu_2O core−shell nanostructures can be applied to nanoparticle systems over a broad overall size range both within and beyond the quasi-static limit. By tailoring the Cu_2O shell thickness, we can selectively tune the light absorption properties of small nanoparticle systems within the quasi-static limit and the light scattering from mesoscopic particles beyond the quasi-static limit. Such selective tuning of scattering vs absorption by tailoring the overall particle size offers new opportunities of achieving optimized optical properties for a variety of applications. For example, the mesoscopic particles are promising for dark-field microscopic bioimaging because of their tunable light scattering properties in the near-infrared water window where tissues and blood are transparent, whereas the smaller particles within the quasi-static limit are more desirable for photothermal therapy due to their highly tunable light absorption in the visible.

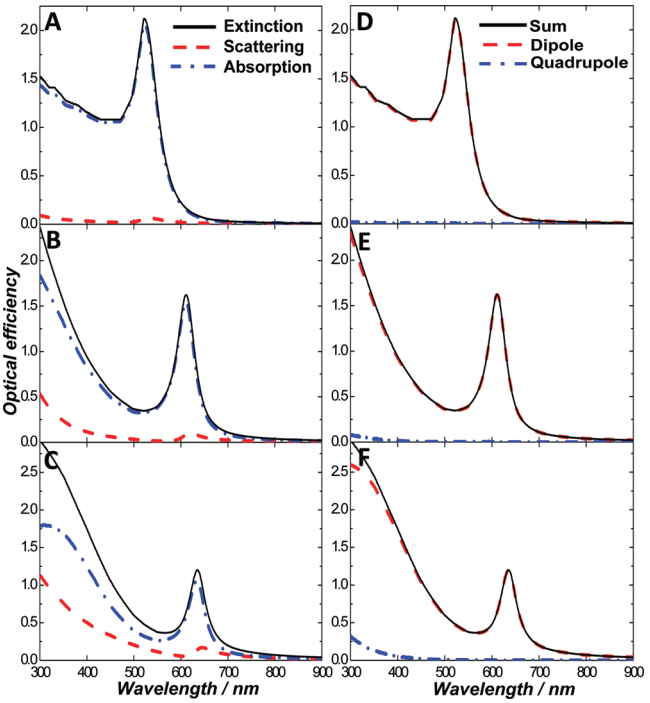

Figure 6. Calculated overall absorption, scattering, and extinction spectra (*left column*) and calculated dipolar and quadrupolar extinction spectra (*right column*) of (A, D) a spherical Au nanoparticle that is 15 nm in radius, (B, E) a Au−Cu_2O core−shell nanoparticle with a core radius of 15 nm and an outer shell radius of 27 nm, and (C, F) a Au−Cu_2O core−shell nanoparticle with a core radius of 15 nm and an outer shell radius of 40 nm. A 1 nm-gap between the Au core and Cu_2O shell is included.

Optical Tunability of Rattle-like Au−Cu_2O Yolk-Shell Nanoparticles. Recently, we observed that polycrystalline Cu_2O nanospheres underwent a symmetric hollowing process at room temperature through which solid spherical particles were converted into thick nanoshells, thin nanoshells, and eventually collapsed shell structures in sequence.[59] Based on our previous studies,[59] this hollowing process was most likely driven by Ostwald ripening of Cu_2O, though the possible involvement of other processes that may facilitate the selective etching of interior of the particles has not been completely ruled out. Here we found that the polycrystalline Cu_2O shells surrounding the Au cores could undergo a similar inside-out hollowing process, which gave rise to the formation of rattle-like Au−Cu_2O yolk-shell nanostructures with engineered nanoscale spacing between the core and the shell.

The structural evolution of the Au−Cu_2O yolk-shell nanoparticles during the hollowing process can be schematically illustrated as shown in Figure 7A. The whole process started from Au−Cu_2O core−shell nanoparticles, and a cavity was created and gradually expanded in size during the inside-out hollowing process. The outer dimension of Cu_2O shell remained

dx.doi.org/10.1021/cm202078t |*Chem. Mater.* 2011, 23, 4587–4598

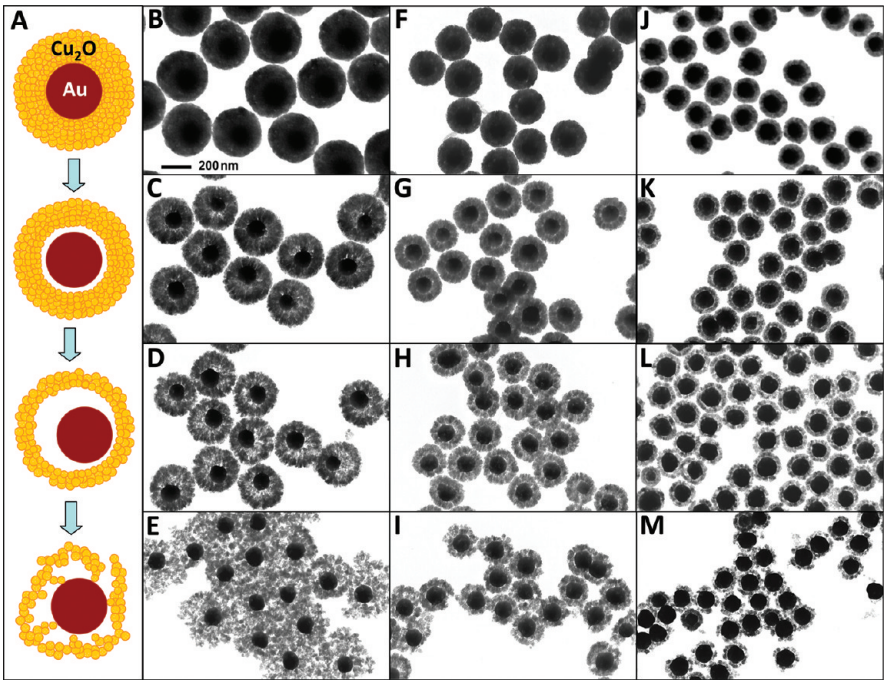

Figure 7. Formation of rattle-like Au−Cu_2O yolk-shell nanoparticles. (A) Schematic illustration of the structural evolution of Au−Cu_2O core−shell nanoparticles during the hollowing of Cu_2O shell. (B-M) Bright-field TEM images showing the structural evolution of Au−Cu_2O core−shell particles with three different outer radii: particles with an average outer radius of 183 nm obtained at (B) 5, (C) 30, (D) 60, and (E) 90 min; particles with an average outer radius of 130 nm obtained at (F) 5, (G) 20, (H) 40, and (I) 60 min; particles with an average outer radius of 98 nm obtained at (J) 5, (K) 20, (L) 40, and (M) 60 min. All TEM images share the same scale-bar in panel B.

the same, while the inner radius became larger gradually, resulting in increased spacing between the core and shell. When the cavity was large enough, the Au core became movable inside Cu_2O shell, giving rise to the formation of asymmetric, rattle-like yolk-shell structures until the shell collapsed on the outer surface of the Au cores when a thin shell limit was reached. The TEM images in Figure 7B-M clearly reveal the structural evolution of Au−Cu_2O yolk-shell particles, and the occurrence of the symmetric hollowing process was observed to be independent upon the original overall size of the starting Au−Cu_2O core−shell particles. Although the symmetric hollowing under the current experimental conditions was observed to be a continuous process, it could be effectively inhibited once the particles were separated from the reaction mixtures through centrifugation and redispersion in ethanol. Therefore we could stop the hollowing process at any time spot to obtain Au−Cu_2O yolk-shell nanoparticles with fine-controlled spacing between the core and shell. No measurable structural changes of the Au−Cu_2O yolk-shell nanoparticles were observed over time periods of several months if the particles were dispersed in ethanol and stored at either room temperature or at 4 °C in refrigerator.

The optical properties of these Au−Cu_2O yolk-shell nanoparticles showed interesting tunability during the structural evolution. As shown in Figure 8A, the colloidal solutions of Au−Cu_2O core−shell nanoparticles (average core radius of 63 nm and outer radius of 130 nm) underwent a dramatic color change during the hollowing process. The experimentally measured extinction spectra of these Au−Cu_2O yolk-shell nanoparticles obtained at different reaction times are shown in Figure 8B. The extinction features in wavelength range from 300 to 600 nm exhibit similar spectral evolution and tunability as those of Cu_2O nanoshells reported in our previous paper,[59] while the dipolar and quadrupolar plasmon resonances of the Au core in the near-infrared progressively blue-shifted as spacing between the Au core and Cu_2O shell increased during Ostwald ripening. The Au−Cu_2O hybrid nanoparticles with collapsed Cu_2O shell structures obtained after 90 min showed very similar plasmonic features as the bare Au nanoparticle cores. A similar trend of spectral evolution has been observed for Au−Cu_2O nanoparticles with different outer radii as shown in Figure S3 in the Supporting Information.

The blue-shift of plasmon resonances during the hollowing process can be interpreted as a result of decrease in the refractive index of medium surrounding the Au cores. The Cu_2O shell surrounding the Au core is not a continuous, single-crystalline shell but polycrystalline and porous in nature. Therefore, small molecules, such as H_2O in the present case, may permeate the Cu_2O shell and fill the hollow space surrounding the Au core created during the hollowing process. This would lead to a significant decrease in the effective refractive index of the local environment surrounding the Au cores, resulting in the blue shift of the Au plasmon resonances. In the present study, we observed that the blue-shift of plasmon resonances were more sensitively dependent on the gap between core and shell when the interior cavity was relatively small but gradually became less sensitive as the size of the interior cavity further increased at later stages during the hollowing process. This is essentially because the plasmon resonances are generally more sensitive to the dielectric medium in closer proximity to the Au nanoparticle surface and become less sensitive to the dielectric medium further away from the nanoparticle. The plasmon resonance sensitivity typically decays over length scales from a few nanometers to several tens of nanometers, depending on the size and geometry of the nanoparticles.[67,77] Change in the dielectric properties of a

dx.doi.org/10.1021/cm202078t |*Chem. Mater.* 2011, 23, 4587–4598

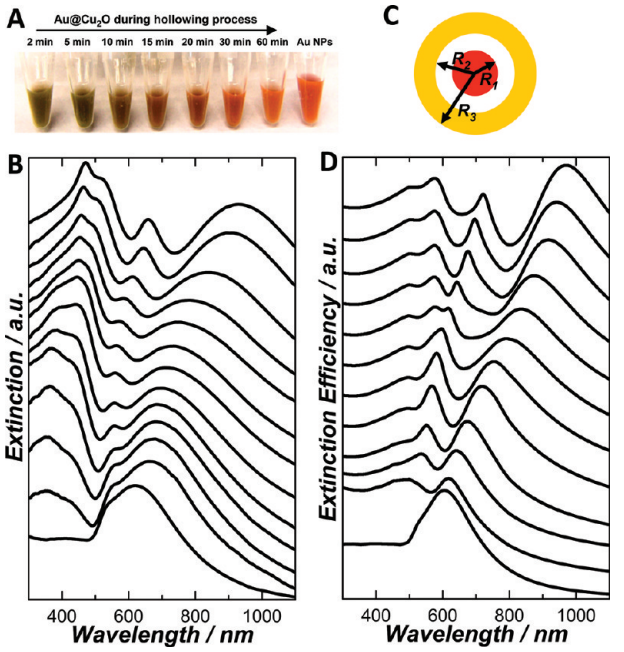

Figure 8. Optical tunability of Au−Cu_2O yolk-shell nanoparticles. (A) Photograph of colloidal suspensions of Au−Cu_2O yolk-shell nanoparticles with an average outer radius of 130 nm obtained at different reaction times during the symmetric hollowing of Cu_2O shells. The right-most sample is bare Au colloids. (B) Experimentally measured extinction spectra of colloidal suspensions of Au−Cu_2O yolk-shell nanoparticles obtained at different reaction times: 2, 5, 10, 15, 20, 25, 30, 40, 50, 60, 75, and 90 min (*from top to bottom*). The bottom spectrum is corresponding to bare Au colloids. (C) Geometry of the Au−Cu_2O composite particle employed for Mie scattering theory calculations. (D) Calculated extinction spectra of a Au−Cu_2O composite particle with fixed R_1 of 63 nm, fixed R_3 of 130 nm, and varying R_2 of 64, 65, 66, 68, 70, 75, 80, 86, 93, 100, and 110 nm (*from top to bottom*). The bottom curve is the calculated spectrum of a spherical Au nanoparticle (63 nm in radius).

medium that is far away from the nanoparticle typically will not introduce significant shift of the plasmon resonance frequencies of the nanoparticle.

To better understand the optical tunability of these yolk-shell nanoparticles, Mie scattering theory calculations have been applied to the symmetric multilayer Au−Cu_2O core−shell nanoparticles with varying interior spacing. Figure 8C shows the geometry of the multilayer particle we simulated, which is a spherically symmetric core−shell particle composed of alternating concentric layers of Au, H_2O, and Cu_2O. The calculated extinction spectra of a Au−Cu_2O particle with fixed R_1 of 63 nm and R_3 of 130 nm but varying R_2 (Figure 8D) show multipeaked extinction line-shapes and geometry-dependent spectral tunability that are in very good agreement with the experimental data. As the spacing between the Au core and Cu_2O shell increases, the plasmon resonances of the Au cores progressively blue-shift and become very similar to the plasmon resonances of bare Au core when the spacing between core and shell is large. At the same time, the extinction features arising from the Cu_2O nanoshells in the visible region also progressively blue-shift as the interior cavity size increases simply due to the decrease of Cu_2O shell thickness.[59]

This approach could also be applied to the controllable fabrication of Ag−Cu_2O core−shell nanoparticles. Panels A-D of Figure S4 in the Supporting Information show a series of TEM images of Ag colloid cores and Ag−Cu_2O core−shell nanoparticles at different stages during the hollowing of Cu_2O shell. As shown in panel E of Figure S4, the coating of 30 nm-radius Ag nanoparticles with a 30 nm-thick Cu_2O nanoshell would shift the plasmon resonance of Ag from ∼430 nm to ∼580 nm. The Ag plasmon resonance was observed to progressively blue-shift as the size of the cavities inside the Cu_2O shells increased (see panel E of Figure S4), which is similar to the trend of Au−Cu_2O core−shell nanoparticles. The experimentally observed extinction line-shapes and spectral evolution during the hollowing process were well reproduced by Mie scattering theory calculations, as shown in panel F of Figure S4, except that the experimentally measured plasmon bands appeared to be much broader than the calculated ones due to the polydispersity of the samples.

CONCLUSIONS

In summary, we have developed a robust wet chemistry approach, which involves the controllable growth of a polycrystalline Cu_2O nanoshell surrounding a Au nanoparticle core and subsequent Ostwald ripening of the Cu_2O shell, for the highly controllable fabrication of Au−Cu_2O hybrid core−shell and rattle-like yolk-shell nanoparticles. We demonstrate that in the Au−Cu_2O hybrid nanoparticles, the plasmonic properties of the Au nanoparticle cores are greatly enriched due to the dielectric properties of the Cu_2O shells. The controllability over several important geometrical parameters of the Au−Cu_2O core−shell nanoparticles, such as Cu_2O shell thickness, size of the Au core, and the spacing between the core and shell, allows us to systematically and selectively fine-tune the synergistic light absorption and scattering properties of the particles over a broad spectral range across the visible and near-infrared regions. We have further performed Mie scattering theory calculations to theoretically interpret the origin of the complexity of extinction spectral line-shapes and geometry-dependent optical tunability of the Au−Cu_2O hybrid nanoparticles. The geometrically tunable optical properties achieved in these Au−Cu_2O core−shell nanoparticles are believed to be crucial and hold great promise to the optimization of a variety of important physical and chemical processes, such as biomedical imaging, photothermal therapy, photocatalysis, optoelectronics, and plasmon-enhanced spectroscopies.

ASSOCIATED CONTENT

Supporting Information. Extinction spectra of Au colloidal nanoparticles with an average radius of 63 nm, dielectric functions of Au, Ag, and Cu_2O, extinction spectral evolution of rattle-like Au−Cu_2O yolk-shell nanoparticles with different outer radii during the hollowing processes, and geometry-dependent optical properties of Ag−Cu_2O yolk-shell nanoparticles. This material is available free of charge via the Internet at http://pubs.acs.org.

AUTHOR INFORMATION

Corresponding Author

*Phone: 803-777-2203. Fax: 803-777-9521. E-mail: wang.hui@chem.sc.edu.

ACKNOWLEDGMENT

H.W. would like to acknowledge the College of Arts and Sciences of University of South Carolina for generous start-up

support and the USC Electron Microscopy Center for instrument use and scientific and technical assistance. The authors would like to thank Naomi Halas of Rice University for providing access to the Mie scattering theory code (written in C^{2+}) based on which the calculations were performed.

REFERENCES

(1) Burda, C.; Chen, X. B.; Narayanan, R.; El-Sayed, M. A. *Chem. Rev.* **2005**, *105* (4), 1025–1102.
(2) Daniel, M. C.; Astruc, D. *Chem. Rev.* **2004**, *104* (1), 293–346.
(3) Jain, P. K.; Huang, X. H.; El-Sayed, I. H.; El-Sayed, M. A. *Acc. Chem. Res.* **2008**, *41* (12), 1578–1586.
(4) Yin, Y.; Alivisatos, A. P. *Nature* **2005**, *437* (7059), 664–670.
(5) Carbone, L.; Cozzoli, P. D. *Nano Today* **2010**, *5* (5), 449–493.
(6) Talapin, D. V.; Lee, J. S.; Kovalenko, M. V.; Shevchenko, E. V. *Chem. Rev.* **2010**, *110* (1), 389–458.
(7) Cortie, M. B.; McDonagh, A. M. *Chem. Rev.* **2011**, *111* (6), 3713–3735.
(8) Costi, R.; Saunders, A. E.; Banin, U. *Angew. Chem., Int. Ed.* **2010**, *49* (29), 4878–4897.
(9) Mokari, T.; Rothenberg, E.; Popov, I.; Costi, R.; Banin, U. *Science* **2004**, *304* (5678), 1787–1790.
(10) Saunders, A. E.; Popov, I.; Banin, U. *J. Phys. Chem. B* **2006**, *110* (50), 25421–25429.
(11) Vaneski, A.; Susha, A. S.; Rodriguez-Fernandez, J.; Berr, M.; Jackel, F.; Feldmann, J.; Rogach, A. L. *Adv. Funct. Mater.* **2011**, *21* (9), 1547–1556.
(12) Formo, E.; Lee, E.; Campbell, D.; Xia, Y. N. *Nano Lett.* **2008**, *8* (2), 668–672.
(13) Dawson, A.; Kamat, P. V. *J. Phys. Chem. B* **2001**, *105* (5), 960–966.
(14) Li, P.; Wei, Z.; Wu, T.; Peng, Q.; Li, Y. D. *J. Am. Chem. Soc.* **2011**, *133* (15), 5660–5663.
(15) Yang, J.; Elim, H. I.; Zhang, Q. B.; Lee, J. Y.; Ji, W. *J. Am. Chem. Soc.* **2006**, *128* (36), 11921–11926.
(16) Shi, W. L.; Zeng, H.; Sahoo, Y.; Ohulchanskyy, T. Y.; Ding, Y.; Wang, Z. L.; Swihart, M.; Prasad, P. N. *Nano Lett.* **2006**, *6* (4), 875–881.
(17) Yu, H.; Chen, M.; Rice, P. M.; Wang, S. X.; White, R. L.; Sun, S. H. *Nano Lett.* **2005**, *5* (2), 379–382.
(18) Pang, M. L.; Hu, J. Y.; Zeng, H. C. *J. Am. Chem. Soc.* **2010**, *132* (31), 10771–10785.
(19) Costi, R.; Saunders, A. E.; Elmalem, E.; Salant, A.; Banin, U. *Nano Lett.* **2008**, *8* (2), 637–641.
(20) Xu, Z. C.; Hou, Y. L.; Sun, S. H. *J. Am. Chem. Soc.* **2007**, *129* (28), 8698–8699.
(21) Chen, W. T.; Yang, T. T.; Hsu, Y. J. *Chem. Mater.* **2008**, *20* (23), 7204–7206.
(22) Tian, Z. Q.; Zhang, Z. L.; Jiang, P.; Zhang, M. X.; Xie, H. Y.; Pang, D. W. *Chem. Mater.* **2009**, *21* (14), 3039–3041.
(23) Li, M.; Yu, X. F.; Liang, S.; Peng, X. N.; Yang, Z. J.; Wang, Y. L.; Wang, Q. Q. *Adv. Funct. Mater.* **2011**, *21*, 1788–1794.
(24) Wang, L. Y.; Luo, J.; Fan, Q.; Suzuki, M.; Suzuki, I. S.; Engelhard, M. H.; Lin, Y. H.; Kim, N.; Wang, J. Q.; Zhong, C. J. *J. Phys. Chem. B* **2005**, *109* (46), 21593–21601.
(25) Zhang, J. T.; Tang, Y.; Lee, K.; Ouyang, M. *Science* **2010**, *327* (5973), 1634–1638.
(26) Lee, J. S.; Shevchenko, E. V.; Talapin, D. V. *J. Am. Chem. Soc.* **2008**, *130* (30), 9673–9675.
(27) Liu, N. G.; Prall, B. S.; Klimov, V. I. *J. Am. Chem. Soc.* **2006**, *128* (48), 15362–15363.
(28) Sun, Z. H.; Yang, Z.; Zhou, J. H.; Yeung, M. H.; Ni, W. H.; Wu, H. K.; Wang, J. F. *Angew. Chem., Int. Ed.* **2009**, *48* (16), 2881–2885.
(29) Yang, Y.; Shi, J. L.; Chen, H. R.; Dai, S. G.; Liu, Y. *Chem. Phys. Lett.* **2003**, *370* (1−2), 1–6.
(30) Murphy, C. J.; San, T. K.; Gole, A. M.; Orendorff, C. J.; Gao, J. X.; Gou, L.; Hunyadi, S. E.; Li, T. *J. Phys. Chem. B* **2005**, *109* (29), 13857–13870.
(31) Link, S.; El-Sayed, M. A. *J. Phys. Chem. B* **1999**, *103* (40), 8410–8426.
(32) Millstone, J. E.; Hurst, S. J.; Metraux, G. S.; Cutler, J. I.; Mirkin, C. A. *Small* **2009**, *5* (6), 646–664.
(33) Skrabalak, S. E.; Chen, J. Y.; Sun, Y. G.; Lu, X. M.; Au, L.; Cobley, C. M.; Xia, Y. N. *Acc. Chem. Res.* **2008**, *41* (12), 1587–1595.
(34) Halas, N. J. *MRS Bull.* **2005**, *30* (5), 362–367.
(35) Wang, H.; Brandl, D. W.; Nordlander, P.; Halas, N. J. *Acc. Chem. Res.* **2007**, *40* (1), 53–62.
(36) Willets, K. A.; Van Duyne, R. P. *Annu. Rev. Phys. Chem.* **2007**, *58*, 267–297.
(37) Mayer, K. M.; Hafner, J. H. *Chem. Rev.* **2011**, *111* (6), 3828–3857.
(38) Snoke, D.; Wolfe, J. P.; Mysyrowicz, A. *Phys. Rev. Lett.* **1987**, *59* (7), 827–830.
(39) Snoke, D. *Science* **1996**, *273* (5280), 1351–1352.
(40) Snoke, D. *Science* **2002**, *298* (5597), 1368–1372.
(41) Jolk, A.; Klingshirn, C. F. *Phys. Status Solidi B* **1998**, *206* (2), 841–850.
(42) Matsumoto, H.; Saito, K.; Hasuo, M.; Kono, S.; Nagasawa, N. *Solid State Commun.* **1996**, *97* (2), 125–129.
(43) Ettema, A.; Versluis, J. *Phys. Rev. B* **2003**, *68* (23), 235101.
(44) Karpinska, K.; Mostovoy, M.; van der Vegte, M. A.; Revcolevschi, A.; van Loosdrecht, P. H. M. *Phys. Rev. B* **2005**, *72* (15), 155201.
(45) Olsen, L. C.; Addis, F. W.; Miller, W. *Sol. Cells* **1982**, *7*, 247–279.
(46) Rai, B. P. *Sol. Cells* **1988**, *25*, 265–272.
(47) Briskman, R. N. *Sol. Energy Mater. Sol. Cells* **1992**, *27* (4), 361–368.
(48) Musa, A. O.; Akomolafe, T.; Carter, M. J. *Sol. Energy Mater. Sol. Cells* **1998**, *51* (3−4), 305–316.
(49) de Jongh, P. E.; Vanmaekelbergh, D.; Kelly, J. J. *Chem. Commun.* **1999**, *12*, 1069–1070.
(50) Hara, M.; Kondo, T.; Komoda, M.; Ikeda, S.; Shinohara, K.; Tanaka, A.; Kondo, J. N.; Domen, K. *Chem. Commun.* **1998**, *3*, 357–358.
(51) Zhang, J. T.; Liu, J. F.; Peng, Q.; Wang, X.; Li, Y. D. *Chem. Mater.* **2006**, *18* (4), 867–871.
(52) Pang, M. L.; Zeng, H. C. *Langmuir* **2010**, *26* (8), 5963–5970.
(53) Yin, M.; Wu, C. K.; Lou, Y. B.; Burda, C.; Koberstein, J. T.; Zhu, Y. M.; O'Brien, S. *J. Am. Chem. Soc.* **2005**, *127* (26), 9506–9511.
(54) Wang, W. Z.; Wang, G. H.; Wang, X. S.; Zhan, Y. J.; Liu, Y. K.; Zheng, C. L. *Adv. Mater.* **2002**, *14* (1), 67–69.
(55) Gou, L. F.; Murphy, C. J. *Nano Lett.* **2003**, *3* (2), 231–234.
(56) Kuo, C. H.; Chen, C. H.; Huang, M. H. *Adv. Funct. Mater.* **2007**, *17* (18), 3773–3780.
(57) Xu, H. L.; Wang, W. Z.; Zhu, W. *J. Phys. Chem. B* **2006**, *110* (28), 13829–13834.
(58) Kuo, C. H.; Huang, M. H. *Nano Today* **2010**, *5* (2), 106–116.
(59) Zhang, L.; Wang, H. *ACS Nano* **2011**, *5* (4), 3257–3267.
(60) Ji, X. H.; Song, X. N.; Li, J.; Bai, Y. B.; Yang, W. S.; Peng, X. G. *J. Am. Chem. Soc.* **2007**, *129* (45), 13939–13948.
(61) Panacek, A.; Kvitek, L.; Prucek, R.; Kolar, M.; Vecerova, R.; Pizurova, N.; Sharma, V. K.; Nevecna, T.; Zboril, R. *J. Phys. Chem. B* **2006**, *110* (33), 16248–16253.
(62) Kuo, C. H.; Hua, T. E.; Huang, M. H. *J. Am. Chem. Soc.* **2009**, *131* (49), 17871–17878.
(63) Kuo, C. H.; Yang, Y. C.; Gwo, S.; Huang, M. H. *J. Am. Chem. Soc.* **2011**, *133* (4), 1052–1057.
(64) Connell, J. G.; Al Balushi, Z. Y.; Sohn, K.; Huang, J. X.; Lauhon, L. J. *J. Phys. Chem. Lett.* **2010**, *1* (23), 3360–3365.
(65) Tian, Z. Q. May 2011, Department of Chemistry, Xiamen University, private communications.
(66) Lu, Y.; Yin, Y. D.; Li, Z. Y.; Xia, Y. N. *Nano Lett.* **2002**, *2* (7), 785–788.
(67) Evanoff, D. D.; White, R. L.; Chumanov, G. *J. Phys. Chem. B* **2004**, *108* (5), 1522–1524.
(68) Salgueirino-Maceira, V.; Caruso, F.; Liz-Marzan, L. M. *J. Phys. Chem. B* **2003**, *107* (40), 10990–10994.

(69) Aslan, K.; Wu, M.; Lakowicz, J. R.; Geddes, C. D. *J. Am. Chem. Soc.* **2007**, *129* (6), 1524–1525.
(70) Ribbing, C. G.; Roos, A., Copper Oxides (Cu_2O, CuO). In *Handbook of Optical Constants of Solids*; Palik, E. D., Ed.; Academic Press: San Diego, 1991; Vol. 2, pp 875−882.
(71) Johnson, P. B.; Christy, R. W. *Phys. Rev. B* **1972**, *6* (12), 4370–4379.
(72) Aden, A. L.; Kerker, M. *J. Appl. Phys.* **1951**, *22* (10), 1242–1246.
(73) Bohren, C. F.; Huffman, D. R. *Absorption and scattering of light by small particles*; Wiley: New York, 1983.
(74) Westcott, S. L.; Jackson, J. B.; Radloff, C.; Halas, N. J. *Phys. Rev. B* **2002**, *66* (15), 155431.
(75) Wang, H.; Halas, N. J. *Adv. Mater.* **2008**, *20* (4), 820–825.
(76) Bardhan, R.; Grady, N. K.; Ali, T.; Halas, N. J. *ACS Nano* **2010**, *4* (10), 6169–6179.
(77) Lal, S.; Grady, N. K.; Goodrich, G. P.; Halas, N. J. *Nano Lett.* **2006**, *6* (10), 2338–2343.